INTERFACE

royalsocietypublishing.org/rsif

Research

Cite this article: Pichler CF, Debastiani R, Mail M, Hein J, Hamann E, Baumbach T, Hölscher H, van de Kamp T. 2026 Multimodal morphological characterization of the femoro-tibial joint of the black vine weevil (*Otiorhynchus sulcatus*). *J. R. Soc. Interface* **23**: 20260376.
https://doi.org/10.1098/rsif.2026.0376

Received: 4 June 2025
Accepted: 19 June 2026

Subject Category:
Life Sciences - Engineering interface

Subject Areas:
biomechanics, biomimetics

Keywords:
bio-tribology, micro-tribology, natural lubricants, weevils, exoskeleton, microstructure, dermal ducts, morphology

Authors for correspondence:
Thomas van de Kamp
e-mail: thomas.vandekamp@kit.edu
Cornelia Friederike Pichler
e-mail: cornelia.pichler@protonmail.com

Supplementary material is available online at https://doi.org/10.6084/m9.figshare.c.8577490.

THE ROYAL SOCIETY PUBLISHING

Multimodal morphological characterization of the femoro-tibial joint of the black vine weevil (*Otiorhynchus sulcatus*)

Cornelia Friederike Pichler[1,2], Rafaela Debastiani[3,4,6], Matthias Mail[3,4,7], Jenny Hein[5], Elias Hamann[5], Tilo Baumbach[2,5], Hendrik Hölscher[1,4] and Thomas van de Kamp[2,5]

[1]Institute of Microstructure Technology (IMT), [2]Laboratory for Applications of Synchrotron Radiation (LAS), [3]Institute of Nanotechnology (INT), [4]Karlsruhe Nano Micro Facility (KNMFi) and [5]Institute for Photon Science and Synchrotron Radiation (IPS), Karlsruhe Institute of Technology (KIT), Eggenstein-Leopoldshafen, Baden-Württemberg, Germany
[6]Helmholtz Institute Freiberg for Resource Technology (HIF), Helmholtz-Zentrum Dresden-Rossendorf (HZDR), Freiberg, Saxony, Germany
[7]TESCAN GmbH, Dortmund, Germany

CFP, 0009-0000-9298-5166; RD, 0000-0003-4396-8612; JH, 0009-0007-4150-4538, EH, 0000-0002-0623-9069; HH, 0000-0002-1033-1669; TvdK, 0000-0001-7390-1318

As open systems, arthropod joints and mechanical articulations face common challenges such as contamination and loss of lubricant. Recent studies suggest that insects manage these objectives of such open joints using a combination of cuticular microstructures and lubricating fluids. Here we provide an insight into the complex internal structure of the femoro-tibial joint of the black vine weevil, *Otiorhynchus sulcatus*. We apply a portfolio of tomography methods, such as X-ray micro- and nano-computed tomography and focused ion beam tomography, to analyse the different hierarchical levels, focusing, in particular, on the cuticle beneath the bearing surface. We provide a description of the gross morphology of the joint, reveal two different types of cuticular canals and document various cuticular surface patterns and microstructures. For the latter, we discuss their possible task in an autonomous cleaning process.

1. Introduction

Insect joints are mechanically diverse and operate as open systems, leading to demanding tribological constraints. Their architecture ranges from simple hinge joints [1] to ball-and-socket configurations [2,3] and even peculiar mechanical analogues such as interlocking gears in the hind trochanters of cicada nymphs [4] and the screw-and-nut-type coxa-trochanteral joint discovered in weevils [5]. Most insect joints are compact mechanical articulations that must reliably transmit forces, guide movement and allow repetitive movement over millions of cycles.

In contrast to vertebrate joints, which are protected from the environment and lubricated by synovial fluid [6–8], insect joints are components of an exoskeleton. Therefore, their friction surfaces are exposed to the environment, which imposes tribological challenges [9,10]. Exposed joints are susceptible

to contamination and abrasive wear. From a mechanical perspective, insect joints can be viewed as integrated tribosystems in which performance depends on several parameters: (i) the gross morphology of the joint partners, which determine contact mechanics; (ii) the microstructure of the cuticular friction surfaces; (iii) the presence and properties of lubricants; and (iv) transport mechanisms of the lubricant to the friction area.

Because many engineered bearings and open mechanical joints encounter constraints similar to those faced by insect joints, the latter became important model systems for biomimetic research [11,12]. Within this context, the insect leg joints are of particular relevance, especially for the design of walking robots and other mobile machines [13–15]. During locomotion, they experience cyclic flexion and extension, shear forces and substrate-induced perturbations, all while remaining exposed to the environment. Among the articulations of the leg, the femoro-tibial joint plays a central mechanical role. Functionally analogous to a knee joint, it supports the whole body and generates a propulsive movement, pushing the body forward [1]. However, the functional design of these joints remains poorly understood [1].

Generally, the femoro-tibial articulation is described as a dicondylar joint with a single degree of freedom [16]. As insects possess antagonistic muscles for flexion and extension of the joint, the articulation is placed medially. The joint can be described as a so-called indirect (suspended) joint [1]. They are widespread in insects and were discovered, e.g. in stick insects (Phasmatodea) [1], katydids (Orthoptera) [17,18] and grasshoppers (Orthoptera) [19]. Two studies [20,21] describe the gross morphology of the femoro-tibial joint of locusts, focusing on the internal microstructures of the semilunar processes, hinting at the common feature of semicircular features to allow extensive movement in one direction. In beetles, it may be modified into a medial hinge joint that is characterized by the transformation of the femoral condyle into a semicircular structure. A tibial impression corresponds to the semicircular femoral condyles. These fit into the tibial concavities, allowing movement along a single axis of rotation [1,22]. Joints with such a distinct morphology were described in *Pachnoda marginata* (Scarabaeidae) [23,24], *Coelorrhina aurata* (Scarabaeidae) [25] and *Zophobas morio* (Tenebrionidae) [1,24] and, therefore, seem to be very common in polyphagan beetles. The jumping legs of *Scirtes hemisphaericus* (Scirtidae) [22] and *Orchestes fagi* (Curculionidae) [26] seem to be reversed with a tibial condyle fitted inside a semicircular femoral concavity. The gross morphology of the tibiotarsal [27] and femoro-tibial [23] joint of *P. marginata* is vastly different but shows the same internal layered microstructure.

When it comes to friction, the microstructure of the cuticular surface of both joint partners at the friction area plays a central role. Microstructures of the cuticle surface in the joint region, such as scale-like, spine-like and sawtooth structures, were shown next to pore openings in the images of previous works [24,25] but have not been thoroughly discussed. A recent study [28] reports on a discovery of cuticular surface microstructures on the membrane of the femoro-tibial joint of the locust *Locusta migratoria*, including scale-like structures, knobs and spines as well as pore channels with an unknown function and mechanosensors. The authors hypothesize a self-cleaning, defensive and friction-reducing function. Oh *et al.* [17,18] compare the microstructures (ridges and smooth) on the contacting surfaces of the femoro-tibial joints of the katydid before and after shearing, showing no signs of wear. They also hypothesize on a possible lubricating substance between the joint partners to reduce wear, supporting the discussed microstructures and complementing elastic moduli.

Though the absence of a sealed cavity prevents a low-viscosity lubrication system similar to vertebrate synovial joints, lubricants in insect joints have been predicted in earlier works [29,30]. Biological viscous protein-based material in the joints of darkling beetles (*Z. morio*) was identified as lubricant [31]. Furthermore, it was shown that the lubricant found in the femoro-tibial joints of the weevil *Otiorhynchus sulcatus* exhibits different drying behaviour and frictional properties than the one found in the scarab beetle *C. aurata* [25].

Apparently, the transport of this lubricant to the frictional surface occurs via canals of 1–5 µm in diameter in the cuticle [24]. Subsequent studies explored this concept in experimental and theoretical work, reaching from imaging lubricants in various joints of different insect species [24] to simulating the lubricant's behaviour and distribution [32–35] as well as tribometer measurements of the joints [35,36]. The functionality of the lubricant is so far inconclusive with studies reporting a roller bearing-like behaviour [31,32,35], while others propose an even distribution [33,34].

Many weevils (Coleoptera: Curculionoidea) are characterized by a highly sclerotized exoskeleton and a tight form closure in their leg joints [37], making them a suitable model system to investigate frictional effects. This inspired us to investigate weevils, focusing on the femoro-tibial hinge joint, as its 'simple' geometry of a flat surface with easily accessible pores opens many possibilities for the application of a variety of characterization methods.

Employing a multimodal approach, we provide an overview of the weevils' femoro-tibial joint. To address the different hierarchical levels of the joint, we used a portfolio of methods well suited to the magnifications required. X-ray micro-computed tomography (µCT) was employed to visualize the entire beetle and to examine the joint's overall morphology. Scanning electron microscopy (SEM) was used to examine the cuticular microstructures. Finally, laboratory-based X-ray nano-computed tomography (nanoCT) and focused ion beam (FIB) provided high-resolution views of the network of internal canals underlying the cuticular surface.

2. Material and methods

2.1. Beetle species

The beetle species examined in this study is the black vine weevil, *O. sulcatus* (Curculionidae: Entiminae; figure 1). Specimens were collected in August 2022, June 2023 and June 2024 in Karlsruhe, Germany.

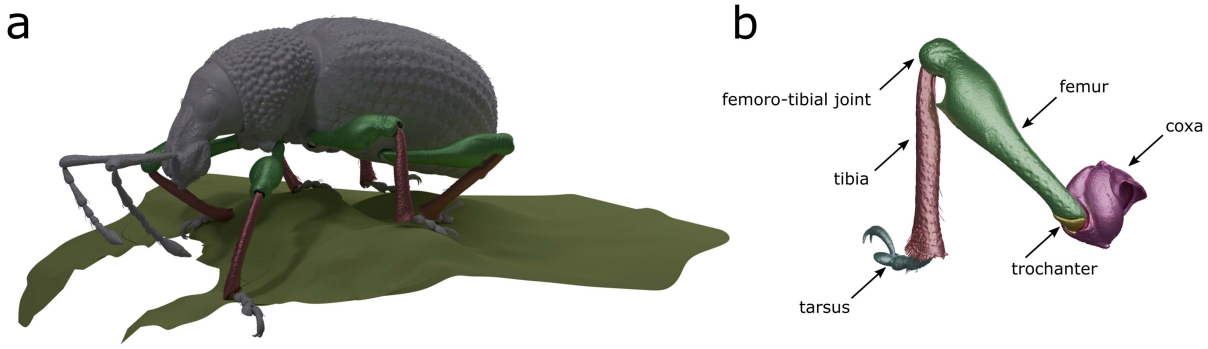

Figure 1. The black vine weevil, *Otiorhynchus sulcatus*: (a) a three-dimensional surface rendering of the beetle with a body length of approximately 8 mm, based on µCT data highlighting the femora in green and the tibiae in red to indicate the joint of interest for this study; (b) a three-dimensional rendering of the right hindleg of the full-body scan with femur in green and tibia in red.

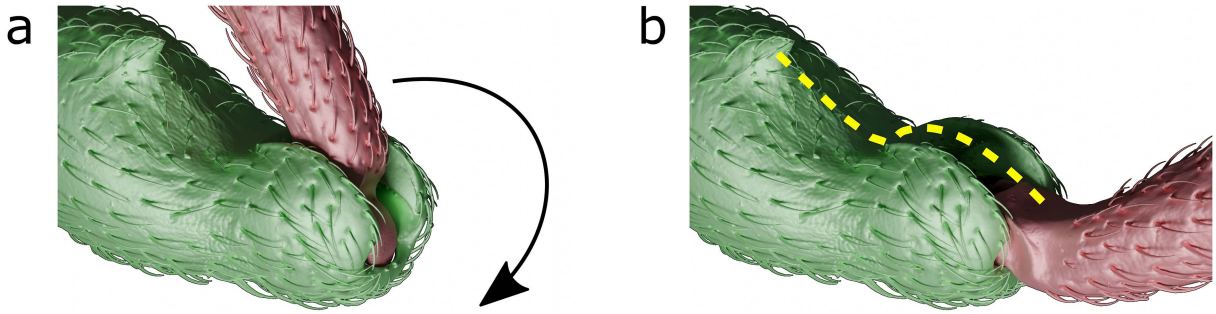

Figure 2. The process of bisecting the femoro-tibial joint is shown with three-dimensional renderings of the µCT data. (a) The joint is rotated into the extended position and beyond to separate the tibia from the femur, and (b) the femur is bisected at the yellow dashed line with a scalpel. The opening and closing of the joint during the movement of the beetle enables many possibilities of contamination, owing to the open nature of the joint.

2.2. X-ray microtomography

X-ray µCT with synchrotron radiation of a sample in 99% ethanol was performed at the IMAGE beamline [38] at the KIT Light Source. We employ a parallel polychromatic X-ray beam, which is spectrally filtered through 10 mm pyrolytic graphite. The resulting spectrum peaked at approximately 17 keV and had a full width at half maximum of approximately 10 keV. We employed two scans at 2× magnification to capture the full specimen and a single scan of the joint region at 10× magnification, resulting in effective pixel sizes of 6.1 and 1.22 µm, respectively. For each scan, we took 200 dark-field images, 200 flat-field images and 3000 equiangularly spaced radiographic projections in a range of 180° with a frame rate of 100 fps (2×) and 70 fps (10×). We used a fast indirect detector system consisting of a scintillator (2×: 200 µm lutetium aluminium garnet (LuAG); 10×: 13 µm terbium-doped lutetium oxyorthosilicate (LSO:Tb)), a white beam microscope with visible light optics (Optique Peter) [39] and a 12-bit pco.dimax high-speed camera (Excelitas PCO GmbH) with 2016 × 2016 pixels of 11 µm physical size.

The control system concert [40] served for automated data acquisition. Data processing, including dark- and flat-field correction and phase retrieval, was performed by the UFO framework [41]. The final tomograms were reconstructed with tofu [42] and yielded phase and absorption contrast datasets. These were blended and converted into 8-bit volumes.

2.3. Scanning electron microscopy

Dissected joints were fixed on SEM stubs, sputtered with a layer of approximately 7 nm of silver and examined with a Supra 60 VP SEM (Zeiss, Germany). In order to obtain clear images of the microstructures without leaving scan marks, the acceleration voltage was limited to 3 keV, and typical working distances of 3–5 mm were used.

The beetle joints used in the SEM measurements were air-dried before bisecting the joint with a scalpel to obtain a clear view of the structures, as shown in figure 2.

2.4. Nano-computed tomography

Beetle joint samples were scanned using the laboratory-based nanoCT Zeiss Xradia 810 Ultra, which employs a Cr anode to produce a quasi-monochromatic X-ray beam with an energy of 5.4 keV. An array of optics is used to achieve a pixel size of 128 nm

within a 65 µm field of view. The samples were scanned using Zernike phase contrast mode with the number of projections and exposure time varying depending on the sample. A total of 901 or 1001 projections were acquired over 180°, with acquisition times of 20 or 40 s per projection. The two-dimensional projections were reconstructed into three-dimensional data using the proprietary software Zeiss Scout and Scan Reconstructor v. 13, which is based on a filtered back-projection algorithm.

The samples for the nanoCT were either air-dried (combined data of five scans), critical point dried (CPD) (combined data of four scans) with isopropanol and CO_2 with an EM CPD300 system (Leica Microsystems, Germany) or chemically dried (combined data of two scans) with 3M™ Novec™ 7100. Samples that were not air-dried were preserved in ethanol prior to drying. The joint was removed from the beetle and bisected, and the region of interest was dissected with a scalpel, before being fixed on a pin to simplify the process of finding the correct area with the limited field of view of the nanoCT, thus reducing the number of scans.

2.5. Focused ion beam tomography

In order to analyse and understand the three-dimensional structure of the pores, samples were prepared and analysed using FIB and SEM. The samples were dissected with a scalpel and then glued to an aluminium stub using carbon stickers. Afterwards, the samples were sputter coated with a thin gold layer to make the sample surface conductive to avoid charging of the samples during SEM analysis. The samples were then transferred to the FIB–SEM-system (TESCAN AMBER). In a first step, a trench was milled using the Ga-ion beam with an acceleration voltage of 30 kV and a beam current of 20 nA. Subsequently, a tomography of the volume of interest was acquired. The data shown in this publication refer to two tomographies. In both cases, an acceleration voltage of 30 kV and a beam current of 10 nA were used to cut the slices. The thickness of each slice was 50 nm. The SEM images were acquired using an acceleration voltage of 5 kV, a beam current of 300 pA and a pixel size of 50 nm. For the first tomography, *ca* 1600 slices were acquired with a height of approximately 46 µm and a width of approximately 44 µm. The second tomography consists of approximately 1400 slices and a height of approximately 57 µm and a width of approximately 73 µm. For each tomography data, three different detector signals were recorded, while for the reconstruction of the three-dimensional information mainly, the signal of the in-chamber Everhart–Thornley secondary electron detector (ET detector) was used.

The beetle joints analysed in the FIB were air-dried to preserve lubricant traces, so that these could be detected in the tomography to reveal the purpose of the pore canals.

2.6. Post-processing of volumetric data

All volumetric data (µCT, nanoCT and FIB) were pre-segmented using Amira 2022.2 (every 10–20 slices depending on the contrast). The pre-segmented labels served as input for smart interpolation with Biomedisa (biomedisa.info) [43]. The results were imported back into Amira, and minor errors were corrected. Subsequently, the surface meshes were generated, which were smoothed and cut using ParaView [44] before being imported, rendered and animated using Blender [45].

3. Results

3.1. Morphology of the joint

The proximal articulation of the tibia is tightly enclosed by the distal femur, forming a hinge joint. The joint itself is nearly symmetrical (see dashed line in figure 2). To permit the hinge joint to move freely, all parts that allow movement with one degree of freedom show a circular geometry (see figures 3 and 4). Viewed from the centre of the circle outwards, the tibia has a concave socket surrounded by the condyle, whereas the femoral side presents a matching condyle encircled by a concave cavity and a raised friction surface. The tibial condyle hooks into the femoral cavity, increasing not only the stability but also the contact surface. The smallest gap is between the tibial frictional surface and the femoral frictional surface in the flexed position. In this area, a high density of pores can be observed (see figure 5).

3.2. Microstructure of the cuticular surface

The tibia part of the femoro-tibial joint exhibits several distinctive cuticular surface patterns (figure 4). Three major types can be distinguished. The first type is located on the ventral side of the tibia and characterized by imbricate scale-like microstructures with denticles on a slightly concave surface (figure 4a). A similar pattern can be found on the tibial condyle. It is located on the outer convex part of the surface, and the denticles develop into microstructures reminiscent of human hands on the inner concave part of the surface (figure 4e). The last pattern type found both on the tibial condyle and the tibial frictional surface features a simple sawtooth structure with anastomoses on an almost flat and convex surface, respectively (figure 4c,d).

The femur part of the femoro-tibial joint exhibits different surface patterns and microstructures (figure 5). It shows an overall circular geometry where the condyle is surrounded by the cavity, followed on one side by the main frictional crescent surface with a sharp edge to the microstructured surface, inhabited again by the simple sawtooth structure with anastomoses in a slightly imbricate fashion (figure 5a). The primary femoral friction surface is characterized by its relatively smooth and flat texture, punctuated by numerous small pore openings. In the thread of the joint (the femoral concavity), other microstructures can be found, based on a sawtooth structure ending in denticles. The microstructures differ in arrangement: straight and parallel (figure 5c) and

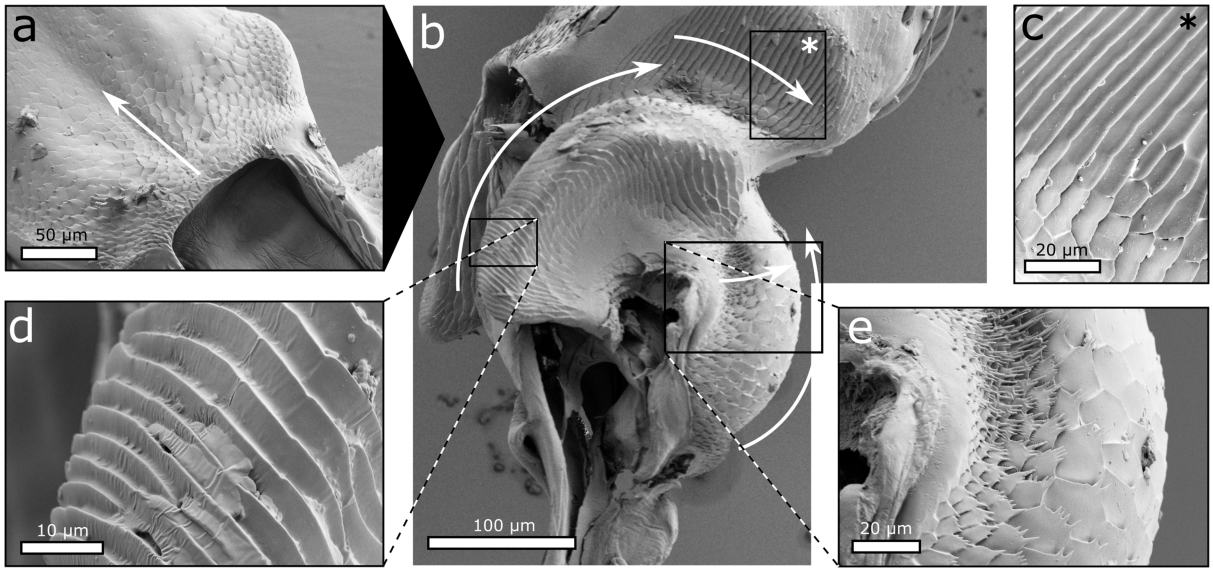

Figure 3. (a) The three-dimensional rendering of the femoral and tibial surface was cut at the respective position; the cuts were translated in the direction of the arrow to allow a less obstructed view of the cuts and µCT slices. (b and c) Two slices of the microtomographic volume showing the tight form fit in the area of the femoral surface where the pores are located. Black arrows indicate the tight gap between the tibia and femur. One can also see the difference between the different cuticle types and structures as well as the pores connecting the haemocoel and the frictional surface (white arrows).

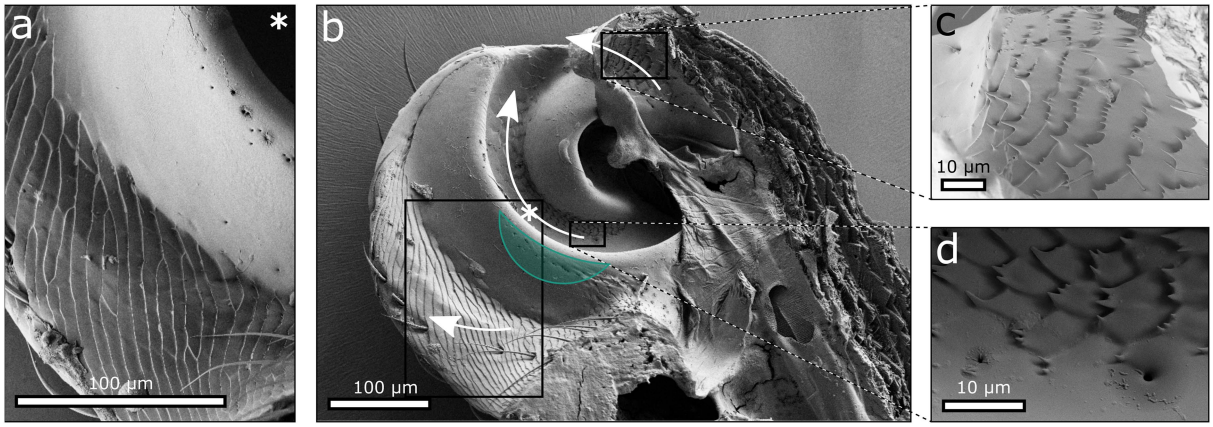

Figure 4. SEM image of the tibia (b) of the femoro-tibial joint of *Otiorhynchus sulcatus*. Zoom-ins show cuticular surface microstructures based on sawtooth structures: an imbricate scale-like structure with denticles on a slightly concave surface (a) evolving into structures reminiscent of human hands on a convex and concave surface (e), an undecorated sawtooth structure, including anastomoses on a flat (c) and convex (d) surface. White arrows indicate the direction of the lower friction, assuming frictional anisotropy, which is common in sawtooth structures.

small scales in an almost isodiametric fashion (figure 5d). Several pores have been observed to exude lubricant. In figure 5, the location of the most accessible pores on the femur of the femoro-tibial joint is marked with a green crescent.

3.3. Canals

The µCT data of the femoro-tibial joint show two types of canals opening to the frictional surfaces. Larger canals (figure 6a) presumably do not open directly into the joint. The smaller canals (figure 6b) are at the limit of the resolution of the µCT and only faintly visible (figure 6c). Both types of canals were only observed in the femur. The structures described in the previous section can also be seen faintly in figure 6a.

To better resolve the internal structure of these canals and confirm their types, we carried out higher-resolution imaging using the nanoCT and FIB tomography approaches previously described.

Both FIB and nanoCT show comparable data (figures 7 and 8), and they distinctly identified two types of canal structures. We will use the generic term 'canal', since our dried specimen did not allow us to determine cells along its surface. The thicker canals originating from the haemocoel and terminating in a bottleneck shape at the frictional surface will be termed bottleneck canals (bc). The narrow canals (nc) that terminate at the frictional surface and originate outside the reasonably possible volume of the FIB and nanoCT measurements will be termed nc. Both pore openings on the frictional surface have a diameter of approximately

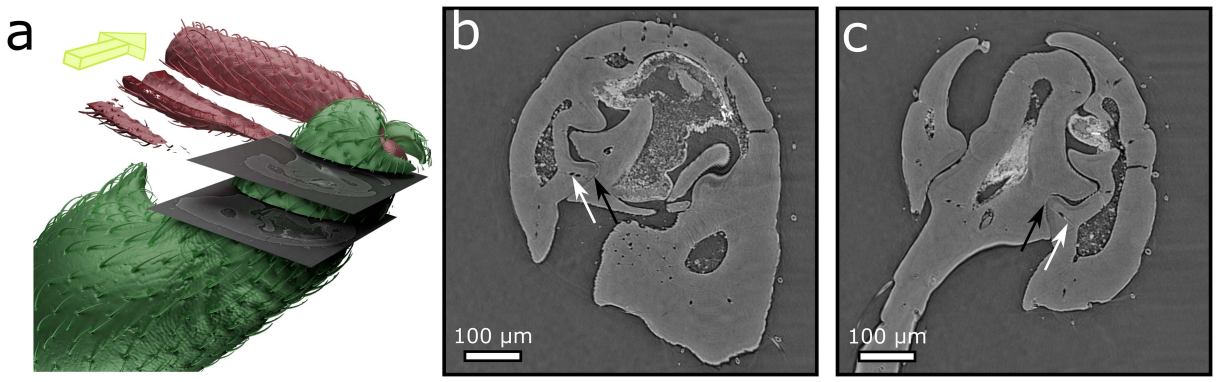

Figure 5. (b) SEM image of the femoral part of the femoro-tibial joint of *Otiorhynchus sulcatus*. Zoom-ins show microstructures resembling sawtooth structures: an imbricate undecorated sawtooth structure with anastomoses next to an unstructured surface (a), an imbricate sawtooth structure with denticles on a concave surface in a parallel fashion (c) and in a scale-like fashion (d). The arrows point in the direction of lower friction based on frictional anisotropy commonly found for sawtooth structures. The green transparent crescent highlights the area of the localized pores exuding lubricant, where the nanoCT and FIB tomographies were performed on separate samples.

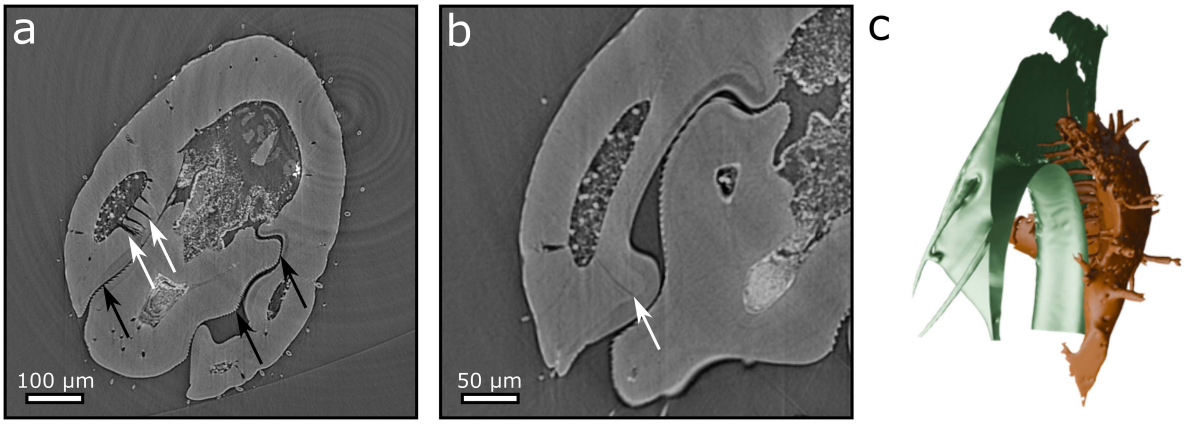

Figure 6. µCT images showing (a) large and (b) narrow canals connecting the frictional surface in the femur (white arrows) to the interior and the microstructures described above, indicated by black arrows. (c) Three-dimensional rendering of the frictional surface of the femur (green) and the haemocoel with connected canals (brown); the cuticle is transparent in this material to avoid obscuring the canals.

1 µm. While the nc do not change their diameter after the pore opening, the bc increase their diameter to approximately 5 µm just below the pore opening to form the bottleneck, decreasing to approximately 1 µm after the voids, and then increase to an almost constant diameter of 7–10 µm, depending on the fusion of multiple bc.

The nanoCT data (chemically dried sample) show two bc (figure 7a) ending in the frictional surface of the femur in the femoro-tibial joint. Below the clear opening to the surface, the beginning of an accumulation of cavities can be seen in white. The nanoCT data also showcase one of the nc (figure 7b), terminating at the frictional surface. In the FIB data (figure 7c,d), bc and nc were visible in proximity to each other. The bc exhibited the same structural characteristics as previously described: a pore opening at the femoral surface that leads into a cavity-rich bottleneck region, which then connects to the interior through a longer canal segment. The three-dimensional renderings (figure 8) of the segmented surface data in both nanoCT and FIB datasets show the disordered arrangement of the network of the canals. The nc can be found both closer and further away from the femoral concavity, as well as in line with and located adjacent to the bc, making it impossible to distinguish them from the outside. In the figures, the frictional surface is depicted in green, while the walls of the canals, haemocoel and cavities are shown in brown.

The nanoCT dataset of the air-dried sample revealed some additional noteworthy features, such as the presence of a duct-like gland structure that terminated in a seta (bristle). This finding suggests the presence of an internal gland opening at a sensory hair. Furthermore, in this specimen, the nc channels were observed to extend approximately parallel to the outer surface of the haemocoel (body cavity) without converging into the haemocoel itself. Two unusual structural features were identified in the nanoCT data. The first was the formation of a distinct loop in the trajectory of an nc, which exhibited a characteristic bend around itself (figure 9). The second was the observation of an nc crossing directly through the haemocoel space as a free-standing tube (figure 9). Owing to the destructive nature of the method, such crossings were not observable with the FIB.

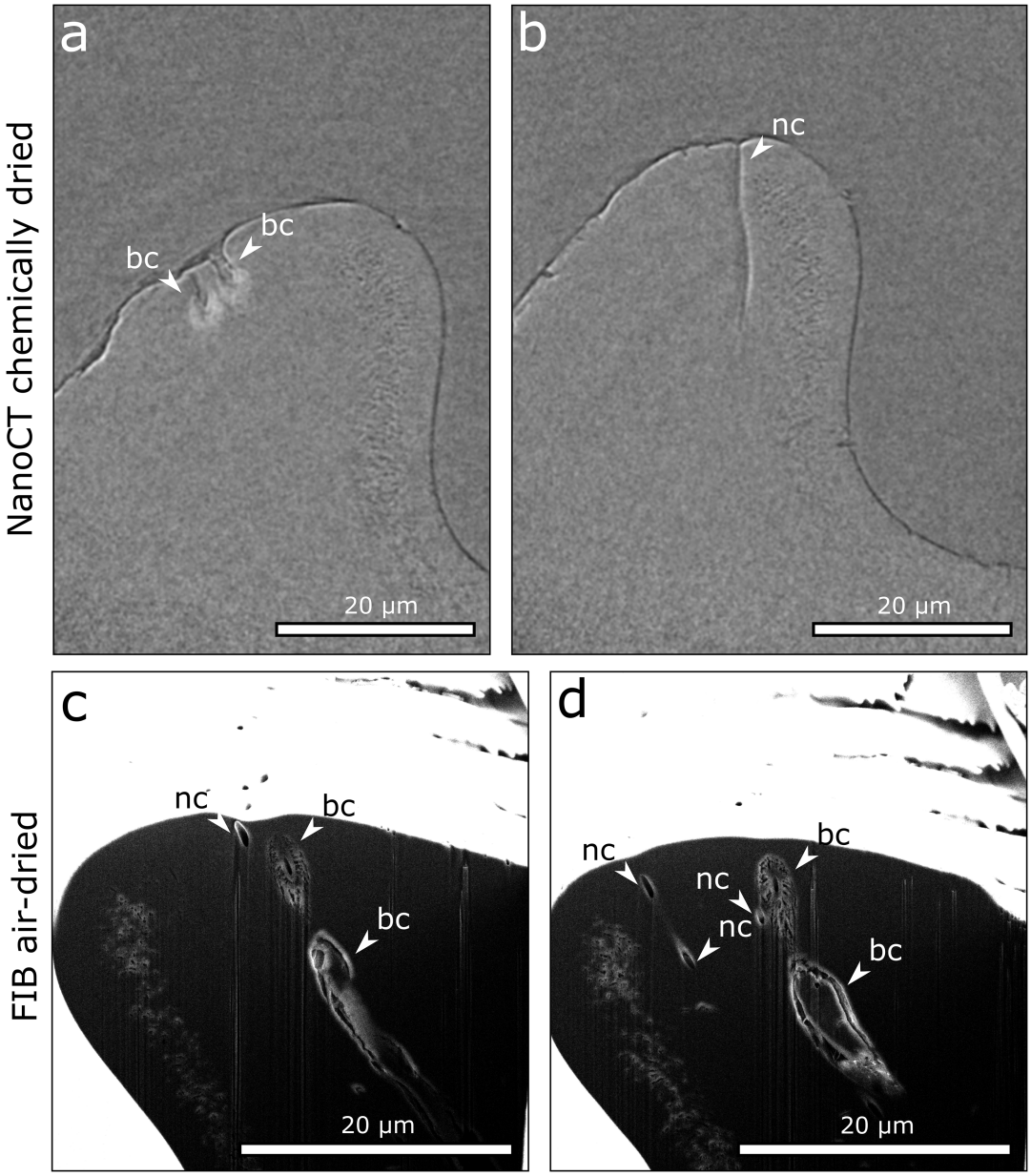

Figure 7. Comparison of nanoCT (chemically dried sample) and FIB slices (air-dried sample): (a) nanoCT slice of two bottleneck canals ending in the frictional surface of the femur; (b) nanoCT slice of a narrow canal ending in the frictional surface of the femur; (c and d) FIB slices of a combination of a bottleneck canal and narrow canals. The bottleneck canal underneath the frictional surface of the femur is surrounded by a collection of cavities. bc – bottleneck canals; nc – narrow canals.

4. Discussion

4.1. Microstructures and their proposed function

The most common surface patterns in arthropods are composed of polygonal/isodiametric microstructures, which may be flat or imbricate and act as scales or scutes [10,46–50]. Their form depends on their function and location [9,46,51]. Such structures generally serve a variety of purposes, including coloration, cleaning and modifying frictional properties of surfaces [29,30,52–54]. The structures vary from sawtooth structures to denticles to bristles [9,48,52,55], which can also be seen in stridulatory organs on the cuticula of e.g. leaf beetles [51,56,57]. Following the classification of cuticular microstructures proposed by Watson *et al.* [58], the microstructures observed here best fit into the category of 'wear and friction control/food grinding/sound generation/body cleaning (mechanical gears)' represented by scale-like surface elements. The common feature of the sawtooth pattern resembles the much smaller pattern found on the scales of the sandfish skink (*Scincus scincus*) and several snakes, where it is associated with frictional anisotropy [59–61] and unidirectional particle transport [62]. These structures cause lower friction in the direction of the sawteeth and higher friction against the sawteeth.

The sawtooth structures described here are most similar to the structures found on the sandfish skink scales, which are simple gradient steps with frayed edges. The sawtooth structures adorned with denticles and the small hand-like projections evoke the

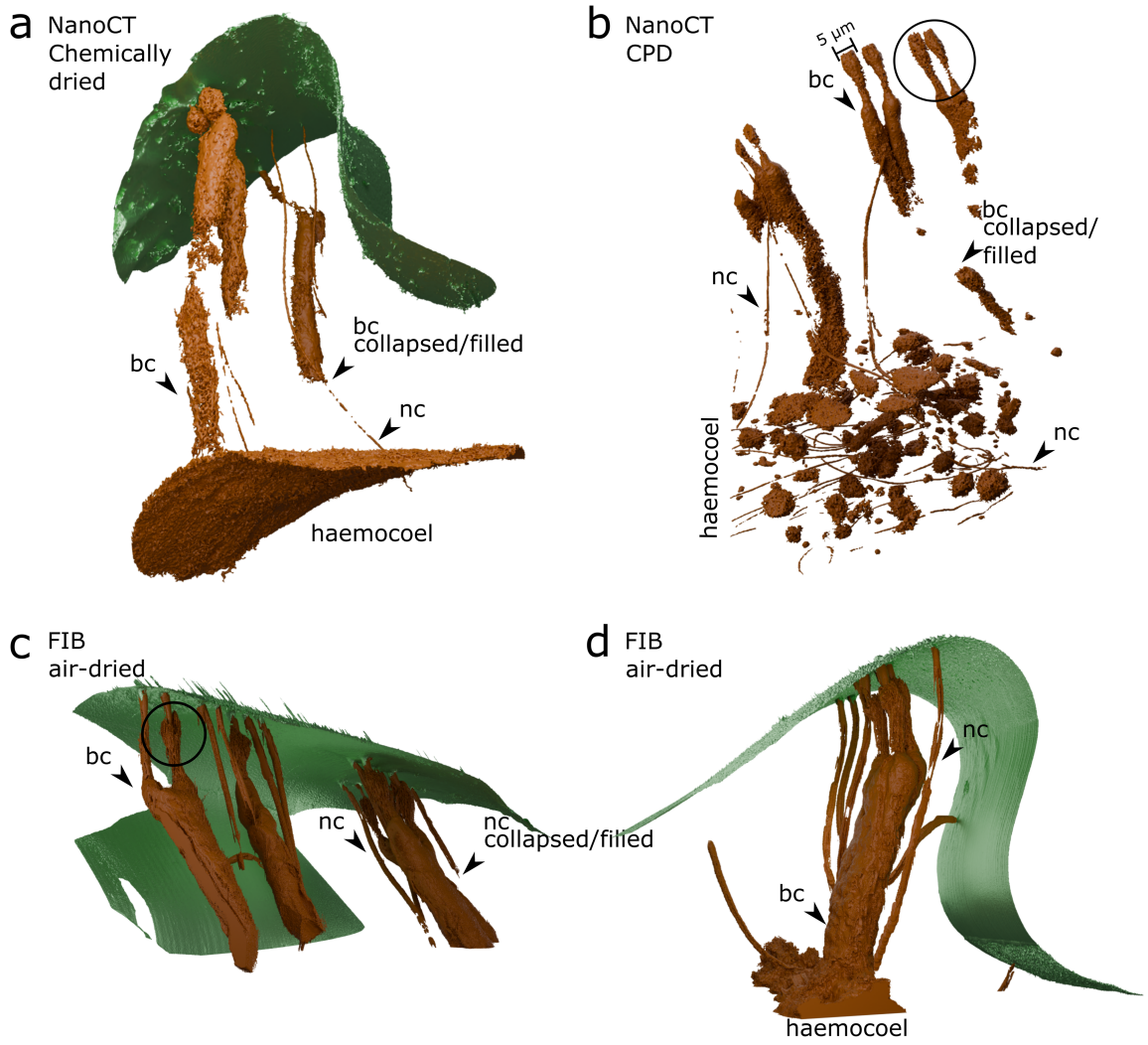

Figure 8. Comparison of three-dimensional renderings (perspective view) of the nanoCT and FIB datasets: (a) nanoCT data of the chemically dried sample, including the frictional surface; (b) nanoCT data of the CPD sample excluding the frictional surface and the walls of the haemocoel to facilitate the view of the network of canals through the haemocoel as well as the remaining collection of voids; (c) FIB data with many canals but an incomplete frictional surface; (d) second FIB dataset with a complete frictional surface. bc – bottleneck canals; nc – narrow canals.

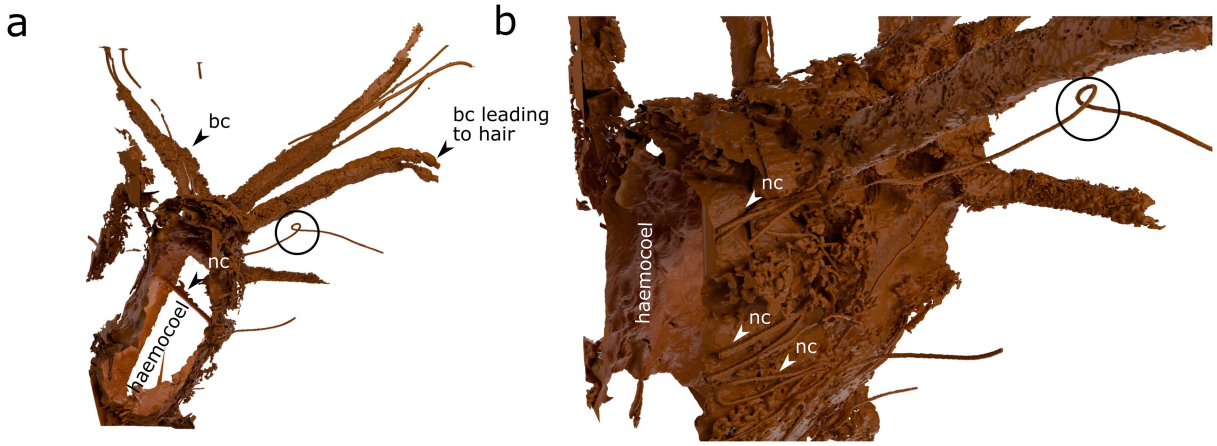

Figure 9. Three-dimensional renderings (perspective view) of the nanoCT data of the air-dried sample. (a) Overview of three-dimensional rendering of the dataset with a collection of bottleneck canals and narrow canals; highlights are the loop in one of the narrow canals (circle), as well as the free-standing narrow canal crossing the haemocoel. (b) Side view of the haemocoel, with narrow canals running parallel to the outside of the haemocoel and a closer look at the looping; bc – bottleneck canals; nc – narrow canals.

more intricate scale microstructures observed in snakes such as the Chinese cobra (*Naja atra*), which feature small finger-like structures on the sawtooth [61]. A notable observation is the consistent orientation of the sawtooth microstructures on the tibial and femoral surfaces, which point in an outward direction on each opposing surface. This alignment suggests that the sawtooth microstructures' function is to channel dirt and debris towards the exterior of the joint. Leg movement probably supports this outward transport, although multiple cycles may be required for the particles to leave the joint (supplementary material, movies). The same process may distribute the lubricant from the pores to the rest of the joint, explaining the high density of the pore openings towards the body and the tight fit of this specific frictional surface. It has been suggested that the joint lubricant itself possesses anti-wear properties, potentially encapsulating abrasive particles before they are expelled from the joint [63]. Three theoretical studies present conflicting results, one of which [33] claims that the semisolid lubricant forms cylindrical logs that function as a rolling bearing owing to the microstructures, while the other two [32,34] claim the formation of lubricant clots. Given the extremely narrow gap between femur and tibia, we favour the interpretation that the lubricant is distributed as a uniform thin layer rather than as rolling cylinders.

It is important to note that both arthropod joints and many engineered systems face challenges associated with lubrication in open environments. Engineers address this using labyrinth seals—intricate arrangements of grooves and ridges retain lubricants while excluding contaminants [64]. The weevil's joint microstructures show conceptual similarity, suggesting a convergent strategy for passive lubrication and debris exclusion.

4.2. Canals

Pore canals and dermal gland ducts can be found throughout arthropod exoskeletons [47,52,65–76]. Often, these canals are modified [77], host a mechanoreceptor connected to sensilla [78–80] or extrude wax on the insect's surface [10,66,72]. A network of canals in insect joints that provide lubricants has been hypothesized as well [29,30,81–83]. Our study supports this hypothesis, revealing two distinct types of canals beneath the joint surface.

Neither the nc nor the bc display a helical nature, small diameter or missing walls such as wax canals (figures 7–9). As the FIB data of helical wax canals [71] show no resemblance, we conclude that neither of them are wax canals.

While the nc resemble single pore canals [31], the bc show similarities to mechanosensitive cells surrounding the setulae found on the elytra of backswimmers of the genus *Notonecta* (Hemiptera) [80]. Although no setae were observed near the pores, the morphology suggests a possible sensory duct. Our research did not reveal the presence of setae on the femoral joint surface in proximity to the pore openings in *O. sulcatus*. However, the observed morphological similarity suggests the possibility of a homologous relationship between the bc and a sensory gland duct, potentially a vestigial or non-seta-associated structure. The canals also resemble Type III dermal duct glands described in the beetle *Tenebrio* [65]. However, the exact classification of these two canal types remains difficult. It is generally believed that insect joint lubrication involves a slow, continuous and uncontrolled release of lubricant [68]. If the bc are linked to a sensory mechanism (e.g. sensing load or motion and actively regulating lubricant release), lubricant release could potentially be modulated rather than purely passive, although this remains speculative.

The nc are undivided and apparently unconnected with very limited changes in diameter, some traversing the haemocoel and some following its periphery. Their origin is unknown. The bc originate in the haemocoel or connected dermal cell and reduce in size towards the surface, sometimes branching in several canals that never directly reach the surface. The pores associated with the bc are separated from the thick canals by an accumulation of small cavities. The details of the lack of fusion of nc and interior and the separation of the bc to their pores by cavities can only be discerned with the nanoCT and FIB. The functional roles of these canals remain unresolved, although a haemolymph-based lubricant is a plausible scenario. This hypothesis is supported by observations in other insects, such as haemolymph extrusion from the femoro-tibial joint in ladybird beetles [9,84]. However, direct evidence is lacking, and sensory functions cannot be excluded.

A major limitation of both FIB and nanoCT is the inability to analyse samples in liquid. For FIB, we examined an air-dried sample sputtered with gold in the hope of detecting residuals of lubricant. As described in a previous study [25], the lubricant undergoes rapid evaporation and cannot be found on desiccated samples. Furthermore, FIB is a destructive method, and any free-standing structures need to be fixated upfront in order to keep them in place during cutting.

Owing to the preparation method of drying the samples for the nanoCT in different ways and cutting them manually with a scalpel, many of the nc as well as some of the bc have collapsed and are no longer distinguishable from the surrounding cuticle.

Therefore, none of the samples show the same degree of preservation as a sample in ethanol as scanned in the µCT. However, FIB and nanoCT are currently the only three-dimensional imaging methods suitable for these samples at this resolution.

4.3. Description of the complete system

µCT data show that the femoro-tibial hinge joint allows a range of motion of up to approximately 90°. Overextension of the joint results in a clean separation of the two joint partners which, even in a dry state, exhibit sufficient elasticity to prevent fracture.

Both femur and tibia contribute structured surfaces to the joint interface. However, pore openings and smooth surfaces are restricted to the femur. All microstructured regions on both sides exhibit sawtooth patterns, probably generating frictional anisotropy that reduces wear and friction, and facilitates self-cleaning by directing contaminants outwards. Two types of canals open into the friction surface, which may serve different roles (e.g. lubrication or sensing).

In contrast to the gross morphology in formerly researched joints of jumping insects (katydids [17,18], *S. hemisphaericus* [22] and *O. fagi* [26]), the femoro-tibial joints of *O. sulcatus* appear to have a tighter form closure. The difference could be explained by

the speed and force needed for the jumping process. Owing to this limited space between the contacting parts, the variety and amount of microstructures within the joint of *O. sulcatus* are surprising as we would expect smooth surfaces for an unobstructed movement. In line with former studies [85], we hypothesize self-cleaning properties of the joint facilitated by the structures to expel intruding contaminants. Lubricants and canals in the joints of insects were first described in 2022 [24,31]. The function of the canals described in our study is still under discussion and will need further research, e.g. by analysis of the contents of the canals in fresh samples or a method combining µCT and nanoCT/FIB with a high-enough resolution, a bigger field of view and fast scan times or the possibility to scan fixed samples.

5. Conclusion

Despite its at-first-sight seemingly simple hinge morphology, the femoro-tibial joint of *O. sulcatus* represents a complex functional system.

By combining SEM, µCT, nanoCT and FIB, we characterized the gross morphology of the joint partners, and the surface microstructures and a complex internal canal system in the femur. Clarifying their functions will require further research, potentially involving *in vivo* experiments or new imaging modalities that can visualize the lubricant *in situ*.

Beyond these primary findings, the unusual looping canal and free-standing canal observed in the nanoCT scans add further complexity to the system. With friction being an indomitable problem in technology and the need for green lubrication, the comparability between the open joints of insects and technical joints and bearings could be of great significance. With the advent of micro-electromechanical systems (MEMS), the need to reduce friction and wear takes on a whole new dimension. A complete picture of existing systems in insects will be very valuable to inspire future technological and tribological developments.

Ethics. This work did not require ethical approval from a human subject or animal welfare committee.

Data accessibility. All data can be found in the institutional repository [86].

Supplementary material is available online [87].

Declaration of AI use. AI was solely used for final light text-polishing and language correction. No data, ideas or results were generated with AI.

Authors' contributions. C.F.P.: conceptualization, data curation, formal analysis, investigation, methodology, visualization, writing—original draft, writing—review and editing; R.D.: data curation, methodology, writing—review and editing; M.M.: data curation, methodology, writing—review and editing; J.H.: data curation, writing—review and editing; E.H.: methodology, software, writing—review and editing; T.B.: resources, writing—review and editing; H.H.: supervision, writing—review and editing; T.v.d.K.: conceptualization, data curation, methodology, project administration, supervision, writing—original draft.

All authors gave final approval for publication and agreed to be held accountable for the work performed therein.

Conflict of interest declaration. We declare we have no competing interests.

Funding. This work was partly carried out with the support of the Karlsruhe Nano Micro Facility (KNMFi, www.knmf.kit.edu), a Helmholtz Research Infrastructure at Karlsruhe Institute of Technology (KIT, www.kit.edu). The Xradia 810 Ultra (nanoCT) core facility was supported by the 3DMM2O – Cluster of Excellence (EXC-2082/1390761711). R.D. acknowledges the support by the Cluster of Excellence 3DMM2O (EXC-2082/1-390761711) funded by the German Research Foundation (DFG).

Acknowledgements. We thank Luisa Maren Borgmann (KIT) for collecting the beetles of the species *Otiorhynchus sulcatus*, Angelica Cecilia (KIT) and Marcus Zuber (KIT) for assistance at the beamline, Tomáš Faragó (KIT) for tomographic reconstruction and István Mikó (University of New Hampshire) for fruitful discussions. C.F.P. acknowledges financial support from the Landesgraduiertenförderung Baden-Württemberg. We acknowledge the KIT Light Source for the provision of instruments at their beamlines and thank the Institute for Beam Physics and Technology (IBPT) for the operation of the Karlsruhe Research Accelerator (KARA). We thank Stefan Hengsbach (KIT) for the provision of the CPD system and drying chemicals.

References

1. Nadein K, Gorb S. 2025 Principal design of the femoro-tibial joint in the main groups of Arthropoda and possible implications for robotics limbs. *Zoomorphology* **144**, 1–17. (doi:10.1007/s00435-025-00708-4)
2. Tajiri R, Misaki K, Yonemura S, Hayashi S. 2011 Joint morphology in the insect leg: evolutionary history inferred from *Notch* loss-of-function phenotypes in *Drosophila*. *Development* **138**, 4621–4626. (doi:10.1242/dev.067330)
3. Frantsevich L, Wang W. 2009 Gimbals in the insect leg. *Arthropod Struct. Dev.* **38**, 16–30. (doi:10.1016/j.asd.2008.06.002)
4. Burrows M, Sutton G. 2013 Interacting gears synchronize propulsive leg movements in a jumping insect. *Science* **341**, 1254–1256. (doi:10.1126/science.1240284)
5. van de Kamp T, Vagovič P, Baumbach T, Riedel A. 2011 A biological screw in a beetle's leg. *Science* **333**, 52. (doi:10.1126/science.1204245)
6. An H, Liu Y, Yi J, Xie H, Li C, Wang X, Chai W. 2022 Research progress of cartilage lubrication and biomimetic cartilage lubrication materials. *Front. Bioeng. Biotechnol.* **10**, 1012653. (doi:10.3389/fbioe.2022.1012653)
7. Jin Z, Dowson D. 2013 Bio-friction. *Friction* **1**, 100–113. (doi:10.1007/s40544-013-0004-4)
8. Merkher Y, Sivan S, Etsion I, Maroudas A, Halperin G, Yosef A. 2006 A rational human joint friction test using a human cartilage-on-cartilage arrangement. *Tribol. Lett.* **22**, 29–36. (doi:10.1007/s11249-006-9069-9)
9. Schmitt M. 2022 *Insektenwunderwelt – Einstieg in die Entomologie*. Wiesbaden, Germany: Springer. (doi:10.1007/978-3-662-64077-7)
10. Neville A. 1975 *Biology of the arthropod cuticle*. Berlin, Germany: Springer. (doi:10.1007/978-3-642-80910-1)
11. Gorb S. 2010 Insect-inspired technologies: insects as a source for biomimetics. In *Insect biotechnology* (ed. A Vilcinskas), pp. 241–264. Berlin, Germany: Springer. (doi:10.1007/978-90-481-9641-8_13)

12. Rajabi H, Wu J, Gorb S. 2021 Insects: functional morphology, biomechanics and biomimetics. *Insects* **12**, 1108. (doi:10.3390/insects12121108)
13. Delcomyn F. 2004 Insect walking and robotics. *Annu. Rev. Entomol.* **49**, 51–70. (doi:10.1146/annurev.ento.49.061802.123257)
14. Noriega Alvarez S, Rojas M, León-Rodríguez H. 2020 Walking robot bio-inspired by insect's locomotion for carbon dioxide diagnostic indexed in the air. In *Proc. 15th Int. Conf. Informatics in Control, Automation and Robotics (ICINCO 2018)*. Porto, Portugal: SciTePress.
15. Dürr V *et al.* 2019 Integrative biomimetics of autonomous hexapedal locomotion. *Front. Neurorobot.* **13**, 88. (doi:10.3389/fnbot.2019.00088)
16. Dirks J. 2025 Insect legs. In *Insect anatomy* (ed. B Moussian), pp. 181–195. Amsterdam, The Netherlands: Elsevier. (doi:10.1016/B978-0-323-85619-5.00003-1)
17. Oh J, Behmer S, Marquess R, Yegin C, Scholar E, Akbulut M. 2017 Structural, tribological, and mechanical properties of the hind leg joint of a jumping insect: using katydids to inform bioinspired lubrication systems. *Acta Biomater.* **62**, 284–292. (doi:10.1016/j.actbio.2017.08.013)
18. Oh J, Yegin C, Akbulut M. 2017 Micro/nanoscale tribological and mechanical investigation of the articular surfaces of katydid leg joints: potential for the novel bioinspired lubrication systems. *MRS Adv.* **2**, 1117–1123. (doi:10.1557/adv.2017.81)
19. Kheireddin B, Williams T, Akbulut M. 2012 Tribological properties of femur-tibia articulation of lubber grasshopper. *Tribol. Int.* **50**, 76–81. (doi:10.1016/j.triboint.2012.02.001)
20. Wan C, Hao Z, Feng X. 2016 Structures, properties, and energy-storage mechanisms of the semi-lunar process cuticles in locusts. *Sci. Rep.* **6**, 35219. (doi:10.1038/srep35219)
21. Chen X, Hao Z. 2021 Microstructure, elastic modulus, and energy storage properties of portion II in the locust semi-lunar process. *AIP Adv.* **11**, 035225. (doi:10.1063/5.0045251)
22. Nadein K, Kovalev A, Gorb S. 2022 Jumping mechanism in the marsh beetles (Coleoptera: Scirtidae). *Sci. Rep.* **12**, 15834. (doi:10.1038/s41598-022-20119-5)
23. Vagts S, Schlattmann J, Kovalev A, Gorb S. 2018 The topology of the leg joints of the beetle *Pachnoda marginata* (Scarabaeidae, Cetoniinae) and its implication for the tribological properties. *Biomimetics* **3**, 12. (doi:10.3390/biomimetics3020012)
24. Nadein K, Gorb S. 2021 Lubrication in the joints of insects (Arthropoda: Insecta). *J. Zool.* **316**, 24–39 (doi:10.1111/jzo.12922)
25. Pichler C, Thelen R, van de Kamp T, Hölscher H. 2025 Friction coefficient evolution of drying lubricant in the joints of beetles by friction force microscopy. *Tribol. Lett.* **73**, 1–10. (doi:10.1007/s11249-025-01963-8)
26. Nadein K, Betz O. 2018 Jumping mechanisms and performance in beetles. II. Weevils (Coleoptera: Curculionidae: Rhamphini). *Arthropod. Struct. Dev.* **47**, 131–143. (doi:10.1016/j.asd.2018.02.006)
27. Vagts S, Schlattmann J, Kovalev A, Gorb S. 2020 Structure and frictional properties of the leg joint of the beetle *Pachnoda marginata* (Scarabaeidae, Cetoniinae) as an inspiration for technical joints. *Biomimetics* **5**, 14. (doi:10.3390/biomimetics5020014)
28. Bruns C, Bekas V, Labisch S, Dirks J. 2025 Cuticular microstructure of the locust femur-tibia joint. *Biol. Open* **14**, bio061934. (doi:10.1242/bio.061934)
29. Scherge M, Gorb S. 2001 *Biological micro- and nanotribology*. Berlin, Germany: Springer.
30. Gorb S, Gorb E. 2019 *Aquatic insects as a source for biomimetics*. Cham, Switzerland: Springer. (doi:10.1007/978-3-030-16327-3)
31. Nadein K, Kovalev A, Thøgersen J, Weidner T, Gorb S. 2021 Insects use lubricants to minimize friction and wear in leg joints. *Proc. R. Soc. B* **288**, 20211065. (doi:10.1098/rspb.2021.1065)
32. Filippov A, Nadein K, Gorb S, Kovalev A. 2024 Large-scale numerical simulation of the solid lubricant behavior in the leg joints of insects. *Adv. Theory Simul.* **7**, 2301236. (doi:10.1002/adts.202301236)
33. Filippov A, Nadein K, Gorb S, Kovalev A. 2024 Biobearings: numerical model of the solid lubricant in the leg joints of insects. *Tribol. Lett.* **72**, 11. (doi:10.1007/s11249-023-01815-3)
34. Filippov A, Nadein K, Gorb S, Kovalev A. 2024 Solid lubricant in the insect leg joints: numerical simulation of tribological properties. *Adv. Theory Simul.* **7**, 2400348. (doi:10.1002/adts.202400348)
35. Putignano C, Nadein K, Thomas J, Gorb S. 2026 Biolubrication in insect joints: a lesson for designing a low-friction micro-bearing. *Acta Biomater.* **214**, 346–354. (doi:10.1016/j.actbio.2026.02.024)
36. Nadein K, Kovalev A, Gorb S. 2024 Tribological properties of the beetle leg joints. *Friction* **12**, 2791–2807. (doi:10.1007/s40544-024-0933-0)
37. van de Kamp T, dos Santos Rolo T, Vagovič P, Baumbach T, Riedel A. 2014 Three-dimensional reconstructions come to life – interactive 3D PDF animations in functional morphology. *PLoS ONE* **9**, e102355. (doi:10.1371/journal.pone.0102355)
38. Cecilia A *et al.* 2025 The IMAGE beamline at the KIT light source. *Synchrotron Radiat.* **32**, 1036–1051 (doi:10.1107/S1600577525003777)
39. Douissard P *et al.* 2012 A versatile indirect detector design for hard X-ray microimaging. *J. Instrum.* **7**, P09016. (doi:10.1088/1748-0221/7/09/P09016)
40. Vogelgesang M, Faragó T, Morgeneyer T, Helfen L, dos Santos Rolo T, Myagotin A, Baumbach T. 2016 Real-time image-content-based beamline control for smart 4D X-ray imaging. *J. Synchrotron Radiat.* **23**, 1254–1263. (doi:10.1107/S1600577516010195)
41. Vogelgesang M, Chilingaryan S, dos Santos Rolo T, Kopmann A. 2012 UFO: a scalable GPU-based image processing framework for on-line monitoring. In *2012 IEEE 14th Int. Conf. on High Performance Computing and Communication & 2012 IEEE 9th Int. Conf. on Embedded Software and Systems*. Liverpool, UK: IEEE.
42. Faragó T, Gasilov S, Emslie I, Zuber M, Helfen L, Vogelgesang M, Baumbach T. 2022 Tofu: a fast, versatile and user-friendly image processing toolkit for computed tomography. *Synchrotron Radiat.* **29**, 916–927. (doi:10.1107/S160057752200282X)
43. Lösel P *et al.* 2020 Introducing Biomedisa as an open-source online platform for biomedical image segmentation. *Nat. Commun.* **11**, 5577. (doi:10.1038/s41467-020-19303-w)
44. Ahrens J, Geveci B, Law C. 2005 ParaView: an end-user tool for large data visualization. In *Visualization handbook* (eds D Hansen, C Johnson), pp. 717–731. Burlington, MA: Elsevier Inc. (doi:10.1016/B978-012387582-2/50038-1)
45. Blender Online Community. 2018 *Blender – a 3D modelling and rendering package*. Amsterdam, The Netherlands: Blender Foundation, Stichting Blender Foundation.
46. Allen R, Ball G. 1979 Synopsis of Mexican taxa of the Loxandrus series (Coleoptera: Carabidae: Pterostichini). *Trans. Am. Entomol. Soc.* **105**, 481–575.
47. Fusco G *et al.* 2000 Cellular processes in the growth of lithobiomorph centipedes (Chilopoda: Lithobiomorpha): a cuticular view. *Zool. Anz.* **239**, 91–102.
48. Krell FT. 1994 Phylogenetic and taxonomic considerations on the variability of cuticular surface micromorphology within one species, Aphodius (Nialus) varians Duftschmid (Insecta: Coleoptera: Scarabaeidae: Aphodiinae). *Rev. Suisse Zool.* **101**, 265–287. (doi:10.5962/bhl.part.79907)
49. Minelli A, Maruzzo D, Fusco G. 2010 Multi-scale relationships between numbers and size in the evolution of arthropod body features. *Arthropod Struct. Dev.* **39**, 468–477. (doi:10.1016/j.asd.2010.06.002)
50. Moretto M, Minelli A, Fusco G. 2015 Cell size versus body size in geophilomorph centipedes. *Sci. Nat.* **102**, 1–9. (doi:10.1007/s00114-015-1269-4)
51. Schmitt M. 1994 The position of the Megalopodinae and Zeugophorinae in a phylogenetic system of the Chrysomeloidea (Insecta: Coleoptera). In *Proc. 3rd Int. Symp. Chrysomelidae*. Beijing: Blackhuys Publishers, Leiden.

52. Schroeder T, Houghtaling J, Wilts B, Mayer M. 2018 It's not a bug, it's a feature: functional materials in insects. *Adv. Mater.* **30**, 1705322. (doi:10.1002/adma.201705322)
53. Hinton H. 1969 Some structures of insects as seen with the scanning electron microscope. *Micron* **1**, 84–108. (doi:10.1016/0047-7206(69)90014-4)
54. Tramsen H, Gorb S, Zhang H, Manoonpong P, Dai Z, Heepe L. 2018 Inversion of friction anisotropy in a bio-inspired asymmetrically structured surface. *J. R. Soc. Interface* **15**, 20170629. (doi:10.1098/rsif.2017.0629)
55. Vilhelmsen L. 2003 Flexible ovipositor sheaths in parasitoid Hymenoptera (Insecta). *Arthropod Struct. Dev.* **32**, 277–287. (doi:10.1016/S1467-8039(03)00045-8)
56. Schmitt M. 1992 Stridulatory devices of leaf beetles (Chrysomelidae) and other Coleoptera. *Adv. Coleopterol.* 263–280. Asociación Europea de Coleopterología, Barcelona.
57. Schmitt M. 1994 Stridulaton in leaf beetles (Coleoptera, Chrysomelidae). In *Novel aspects of the biology of Chrysomelidae*. (eds PH Jolivet, ML Cox, E Petitpierre), pp. 319–325. Dordrecht, The Netherlands: Springer. (doi:10.1007/978-94-011-1781-4_25)
58. Watson G, Watson J, Cribb B. 2017 Diversity of cuticular micro- and nanostructures on insects: properties, functions, and potential applications. *Annu. Rev. Entomol.* **62**, 185–205. (doi:10.1146/annurev-ento-031616-035020)
59. Hazel J, Stone M, Grace M, Tsukruk V. 1999 Nanoscale design of snake skin for reptation locomotions via friction anisotropy. *J. Biomech.* **32**, 477–484. (doi:10.1016/S0021-9290(99)00013-5)
60. Wu W, Lutz C, Mersch S, Thelen R, Greiner C, Gomard G, Hölscher H. 2018 Characterization of the microscopic tribological properties of sandfish (*Scincus scincus*) scales by atomic force microscopy. *Beilstein J. Nanotechnol.* **9**, 2618–2627. (doi:10.3762/bjnano.9.243)
61. Wu W, Yu S, Schreiber P, Dollmann A, Lutz C, Gomard G, Greiner C, Hölscher H. 2020 Variation of the frictional anisotropy on ventral scales of snakes caused by nanoscale steps. *Bioinspir. Biomim.* **15**, 056014. (doi:10.1088/1748-3190/ab9e51)
62. Wu W, Guttmann M, Schneider M, Thelen R, Worgull M, Gomard G, Hölscher H. 2021 Snake-inspired, nano-stepped surface with tunable frictional anisotropy made from a shape-memory polymer for unidirectional transport of microparticles. *Adv. Funct. Mater.* **31**, 2009611. (doi:10.1002/adfm.202009611)
63. Nadein K, Gorb S. 2024 Abrasive wear in the leg joints of insects. *Adv. Mater. Interfaces* **11**, 2300743. (doi:10.1002/admi.202300743)
64. Khonsari M, Booser E. 2017 *Applied tribology – bearing design and lubrication*. New York, NY: John Wiley & Sons. (doi:10.1002/9781118700280)
65. Noirot C, Quennedey A. 1974 Fine structure of insect epidermal glands. *Annu. Rev. Entomol.* **19**, 61–80. (doi:10.1146/annurev.en.19.010174.000425)
66. Hadley N. 1982 Cuticle ultrastructure with respect to the lipid waterproofing barrier. *J. Exp. Zool.* **222**, 239–248. (doi:10.1002/jez.1402220306)
67. Foldi I. 1991 The wax glands in scale insects: comparative ultrastructure, secretion, function and evolution (Homoptera: Coccoidea). *Ann. Soc. Entomol. Fr. (N.S.)* **27**, 163–188. (doi:10.1080/21686351.1991.12277633)
68. Foster S, Casas J. 2024 How insect exocrine glands work. *Annu. Rev. Entomol.* **70**, 65–82.
69. Gorb S. 1997 Porous channels in the cuticle of the head-arrester system in dragon/damselflies (Insecta: Odonata). *Microsc. Res. Tech.* **37**, 583–591. (doi:10.1002/(SICI)1097-0029(19970601)37:5/6⟨583::AID-JEMT18⟩3.3.CO;2-L)
70. Hadley N. 1986 The arthropod cuticle. *Sci. Am.* **255**, 104–113. (doi:10.1038/scientificamerican0786-104)
71. Li D, Guo J, Wang X, Moussian B, Zhang C. 2021 Three-dimensional reconstruction of pore canals in the cuticle of the brown planthopper. *Sci. China Life Sci.* **64**, 1992–1994. (doi:10.1007/s11427-020-1857-7)
72. Locke M. 1961 Pore canals and related structures in insect cuticle. *J. Cell Biol.* **10**, 589–618. (doi:10.1083/jcb.10.4.589)
73. Lococo D, Huebner E. 1980 The ultrastructure of the female accessory gland, the cement gland, in the insect *Rhodnius prolixus*. *Tissue Cell* **12**, 557–580. (doi:10.1016/0040-8166(80)90045-2)
74. Ruangchai S, Reisecker C, Hild S, Ziegler A. 2013 The architecture of the joint head cuticle and its transition to the arthrodial membrane in the terrestrial crustacean *Porcellio scaber*. *J. Struct. Biol.* **182**, 22–35. (doi:10.1016/j.jsb.2013.01.009)
75. Sombke A, Müller C. 2021 When SEM becomes a deceptive tool of analysis: the unexpected discovery of epidermal glands with stalked ducts on the ultimate legs of geophilomorph centipedes. *Front. Zool.* **18**, 1–19. (doi:10.1186/s12983-021-00402-3)
76. Zhang L, Wang S, Billen J, Wei C. 2021 Morphology and ultrastructure of the epithelial femoral gland in cicadas (Hemiptera: Cicadidae). *Arthropod Struct. Dev.* **64**, 101086. (doi:10.1016/j.asd.2021.101086)
77. Halcrow K. 1978 Modified pore canals in the cuticle of *Gammarus* (Crustacea: Amphipoda); a study by scanning and transmission electron microscopy. *Tissue Cell* **10**, 659–670. (doi:10.1016/0040-8166(78)90053-8)
78. Guo J, Wang X, Li D, Song D, Zhang C. 2020 Three-dimensional architecture of a mechanoreceptor in the brown planthopper, *Nilaparvata lugens*, revealed by FIB-SEM. *Cell Tissue Res.* **379**, 487–495. (doi:10.1007/s00441-019-03122-7)
79. Steinbrecht R. 1997 Pore structures in insect olfactory sensilla: a review of data and concepts. *Int. J. Insect Morphol. Embryol.* **26**, 229–245. (doi:10.1016/S0020-7322(97)00024-X)
80. Mail M *et al.* 2018 A new bioinspired method for pressure and flow sensing based on the underwater air-retaining surface of the backswimmer *Notonecta*. *Beilstein J. Nanotechnol.* **9**, 3039–3047. (doi:10.3762/bjnano.9.282)
81. Billen J. 2009 Occurrence and structural organization of the exocrine glands in the legs of ants. *Arthropod Struct. Dev.* **38**, 2–15. (doi:10.1016/j.asd.2008.08.002)
82. Billen J, Vander Plancken L. 2014 Exocrine glands in the legs of the stingless bee *Frieseomelitta varia* (Lepeletier) (Apidae: Meliponini). *Sociobiology* **61**, 386–392. (doi:10.13102/sociobiology.v61i4.386-392)
83. Nijs C, Billen J. 2015 Exocrine glands in the legs of the social wasp *Vespula vulgaris*. *Arthropod Struct. Dev.* **44**, 433–443. (doi:10.1016/j.asd.2015.08.011)
84. Knapp M, Dobeš P, Řeřicha M, Hyršl P. 2018 Puncture vs. reflex bleeding: haemolymph composition reveals significant differences among ladybird species (Coleoptera: Coccinellidae), but not between sampling methods. *Eur. J. Entomol.* **115**, 1–6. (doi:10.14411/eje.2018.001)
85. Nadein K, Gorb S. 2022 Smart joints: auto-cleaning mechanism in the legs of beetles. *Commun. Biol.* **5**, 1030. (doi:10.1038/s42003-022-03924-6)
86. Pichler C, Debastiani R, Mail M, Hein J, Hamann E, Baumbach T, Hölscher H, van de Kamp T. 2026 Tomographic data of the weevil. *Otiorhynchus sulcatus* [Dataset]. Karlsruhe Institute of Technology. (doi:10.35097/AA76QR904SDZ91RA)
87. Pichler CF, Debastiani R, Mail M, Hein J, Hamann E, Baumbach T, Höelscher H, van de Kamp T. 2026 Supplementary material from: Multimodal morphological characterization of the femoro-tibial joint of the black vine weevil (*Otiorhynchus sulcatus*). Figshare. (doi:10.6084/m9.figshare.c.8577490)